Makara Journal of Science

Volume 27
Issue 2 *June*

Article 6

6-25-2023

TiO2 Crystallization at Room Temperature and Preparation of Transparent Carbon Counter Electrode for Low-Cost Dye-Sensitized Solar Cells

Muhammad Iqbal Syauqi
Department of Chemistry, Faculty of Mathematics and Natural Sciences, Universitas Indonesia, Depok 16424, Indonesia, muhammad.iqbal@sci.ui.ac.id

Afiten Rahmin Sanjaya
Department of Chemistry, Faculty of Mathematics and Natural Sciences, Universitas Indonesia, Depok 16424, Indonesia

Mohammad Jihad Madiabu
Department of Chemical Analysis, Politeknik AKA Bogor, Bogor 16154, Indonesia

Munawar Khalil
Department of Chemistry, Faculty of Mathematics and Natural Sciences, Universitas Indonesia, Depok 16424, Indonesia

Jarnuzi Gunlazuardi
Department of Chemistry, Faculty of Mathematics and Natural Sciences, Universitas Indonesia, Depok 16424, Indonesia

Recommended Citation

Syauqi, Muhammad Iqbal; Sanjaya, Afiten Rahmin; Madiabu, Mohammad Jihad; Khalil, Munawar; and Gunlazuardi, Jarnuzi (2023) "TiO2 Crystallization at Room Temperature and Preparation of Transparent Carbon Counter Electrode for Low-Cost Dye-Sensitized Solar Cells," *Makara Journal of Science*: Vol. 27: Iss. 2, Article 6.
DOI: 10.7454/mss.v27i2.1476
Available at: https://scholarhub.ui.ac.id/science/vol27/iss2/6

Makara Journal of Science, 27/2 (2023), 129–139
doi: 10.7454/mss.v27i2.1476

TiO_2 Crystallization at Room Temperature and Preparation of Transparent Carbon Counter Electrode for Low-Cost Dye-Sensitized Solar Cells

Muhammad Iqbal Syauqi[1*], Afiten Rahmin Sanjaya[1], Mohammad Jihad Madiabu[2], Munawar Khalil[1], and Jarnuzi Gunlazuardi[1]

1. Department of Chemistry, Faculty of Mathematics and Natural Sciences, Universitas Indonesia, Depok 16424, Indonesia
2. Department of Chemical Analysis, Politeknik AKA Bogor, Bogor 16154, Indonesia

[*]*E-mail: Muhammad.iqbal@sci.ui.ac.id*

Received December 2, 2022 | Accepted April 2, 2023

Abstract

We developed a low-cost dye-sensitized solar cell (DSSC) using TiO_2 fabricated via rapid breakdown anodization (RBA) and ultrafast room-temperature crystallization (URTC). The prepared TiO_2 was deposited on a self-made fluorine-doped tin oxide (FTO) conductive glass, and the FTO/TiO_2 system was sensitized using curcumin dye. The DSSC was constructed by sandwiching the FTO/TiO_2/curcumin electrode with an I^-/I_2 electrolyte and a transparent carbon counter electrode prepared using a liquid–liquid interface system. The characterization results showed that the TiO_2 freshly prepared via URTC was transformed into an anatase crystalline phase, which exhibited a 3.10 eV band gap and a 10.08 nm average crystallite size, comparable to those of the TiO_2 prepared via the conventional 450 °C annealing treatment (3.13 eV, 11.60 nm). The photocurrent activity of the URTC-prepared TiO_2 under ultraviolet light (0.10 mA/cm^2) was also comparable to that of the annealed TiO_2 (0.12 mA/cm^2). In addition, a transparent carbon electrode (FTO/C_t) was prepared successfully; it exhibited a ±58.26% transparency under visible light and comparable electrocatalytic activity to Pt-coated FTO. The DSSC based on FTO/TiO_2-URTC/curcumin and FTO/C_t showed front and back illumination efficiencies of 0.47% and 0.26%, respectively. These results are only slightly lower than those of the conventional DSSC with FTO/annealed TiO_2/curcumin//FTO/Pt, which exhibited front and back illumination efficiencies of 0.52% and 0.36%, respectively.

Keywords: dye-sensitized solar cell, rapid breakdown anodization, transparent carbon counter electrode, ultrafast room-temperature crystallization

Introduction

The energy and environmental crises have led to a massive increase in the use of solar cells worldwide. Silicon-based solar cells, with an average efficiency output of ~20%, currently lead the market owing to their mature technology [1]. However, the solar cells still feature several drawbacks, such as high cost, complicated and energy-consuming production processes [2], and reduced efficiency under high temperatures [3]. Furthermore, developing alternative solar cells is crucial owing to the possibility of limited resources and increased demand. Dye-sensitized solar cells (DSSCs) as third-generation solar cells have attracted attention as a possible alternative owing to their simple, low-cost, and environmentally friendly fabrication process and promising solar-to-electrical energy conversion efficiency [4]. Moreover, the DSSC device can outperform silicon solar cells under high-temperature and low-light-intensity conditions [5]. However, the use of large-scale DSSCs is not attractive because despite their low production costs, their output efficiency is not comparable to that of silicon-based solar cells. The highest reported photoelectric efficiency of DSSCs is 16.5% (observed by the Hou group [6]), followed by 14.3% (observed by the Kakiage group [7]), with almost all of the reports emphasizing the modification of the adopted sensitizer. Researchers have aimed to reach a theoretical DSSC efficiency of 20.25% for single cells and 43% for tandem cells [8,9].

Another interesting research area is reducing the production cost of DSSCs to reach more competitive cents/kWh. The common DSSCs comprise a sensitized semiconductor photoanode, an I^-/I_2 redox couple electrolyte, and a counter electrode. The counter electrode is one of the crucial components accounting for the DSSC cost, as platinum, the conventionally used

material, is scarce and expensive. A carbon-based counter electrode is an interesting alternative owing to its low cost, comparable conductivity to platinum, and controllable surface area [10, 11]. However, its dark color does not allow for back-irradiation on the DSSCs, and its adhesion to the glass substrate limits its lifespan. These drawbacks can be reduced by fabricating a transparent carbon conductive layer. Souza *et al*. reported their success in fabricating conductive carbon layers from numerous carbon sources via the liquid–liquid interface technique. This technique is easy to perform, and the fabricated carbon-based material performed well as a working electrode in the electropolymerization reaction of aniline [12].

The involvement of numerous heating processes also needs to be addressed to reduce the cost of DSSCs. Particularly, in the photoanode, a semiconductor such as TiO_2, ZnO, or SnO_2 in the crystalline form is used as a charge separator and a dye adsorber [13–15]. The crystallization process usually occurs under high temperatures of 400–700 °C, resulting in high energy consumption and costs. Energy consumption can be reduced by crystallizing the semiconductor using hot water or water vapor. This technique has been used to convert amorphous TiO_2 powder and nanotube to anatase form. Because the process is relatively fast, this technique is called ultrafast room-temperature crystallization (URTC) [16, 17].

Despite the potential of low-temperature-crystallized TiO_2, the report on the use of such TiO_2 and transparent carbon electrodes in DSSC fabrication is still scarce. Hence, this paper presents DSSC preparation using a TiO_2 photoanode crystallized at low temperatures and a transparent graphite layer as the counter electrode. The amorphous TiO_2 was synthesized via the rapid breakdown anodization (RBA) technique using Ti metal, to obtain a large-surface-area tubular TiO_2 [18, 19]. Through chemical vapor deposition using a nebulizer spray, a conductive fluorine-doped tin oxide (FTO) glass was also fabricated as the base substrate to be coated by TiO_2 and transparent carbon (C_t) [20]. Curcumin natural dye was used as the sensitizer, while I^-/I_2 in acetylacetone was used as an electrolyte.

Materials and Methods

Materials. Titanium foils (99.78% purity, 0.2 mm thickness) were obtained from Sigma Aldrich and used as obtained. The anodization process was conducted using a VOM 6005E DC power supply. $HClO_4$, $SnCl_2.2H_2O$, HCl, HF, $K_3Fe(CN)_6$, KCl, ethanol, acetone, and isopropyl alcohol were purchased from Merck. The deionized (DI) water used in all experiments was obtained from Merck Milli-Q Direct Water. The performance of the modified electrode was measured using the EdaQ potentiostat. To measure the photoresponse, a 12 W blacklight lamp and a wolfram lamp were used to emit ultraviolet (UV) and visible (vis) lights, respectively.

Fabrication of FTO glass using a nebulizer spray. The conductive glass used in the solar cell was made by depositing FTO on silica glass using a nebulizer spray [20]. The silica glass substrate was cleaned using a detergent solution, acetone, and ethanol before being heated at 200 °C for 10 min and at 520 °C for 30 min. The precursor solution was made by mixing 16.92 g of $SnCl_2{\cdot}2H_2O$ with 5 mL of concentrated HCl. The mixture was heated until the volume was reduced by half, and then 0.4 mL of HF and methanol were added until the volume reached 20 mL. The solution was then introduced into the nebulizer, and the steam formed at a flow rate of 0.4 mL/min was directed onto the glass substrate in the furnace for 2 min. The glass was heated at 520 °C for 10 min. This coating process was done eight times to obtain the desirable FTO properties.

Synthesis of TiO_2 via RBA and URTC. TiO_2 powder was synthesized via the RBA technique, using a titanium plate and perchloric ion electrolyte [18]. The titanium plate (0.8 × 45 × 10 mm) was cleaned up using 1000 cc and 1500 cc sandpaper and then sonicated in acetone, ethanol, isopropyl alcohol, and DI water for 30 min each. After the cleaning process, the titanium plate was dried at 80 °C and then applied as a working electrode for the RBA technique, with 0.15 M $HClO_4$ in distilled water as the electrolyte and stainless steel foil as the counter electrode. The anodization process was conducted under a 15 V direct current and room temperature (25–30 °C), with a distance of 10 mm between both electrodes. The current response over time was recorded until all parts of the titanium plate were converted to white powder (TiO_2). The TiO_2 formed then was rinsed using DI water until it was free from acid and chloride, and then dried at 60 °C for 24 h. The amorphous TiO_2 was crystallized via URTC by exposing the powder to water vapor from water boiled in an opened reactor for 3 h [17]. The processed sample was labeled TiO_2u. For comparison, a TiO_2 sample was also crystallized via the common annealing method (heating at 450 °C for 3 h) and labeled TiO_2a. The TiO_2 photoanode was prepared via deposition of the TiO_2 paste in acetylacetone, water, and triton X. The deposition to the FTO was conducted via the doctor blade method. The film was then sintered on the hotplate at 450 °C for 1 h to cause the TiO_2 paste to stick to the FTO.

Deposition of transparent carbon on FTO as the counter electrode. A transparent carbon (C_t) layer was synthesized from graphite using the liquid–liquid interface technique [21]. First, 1 mg of dried graphite powder was diluted in 100 mL toluene with 60 min of ultrasonication. Then, DI water was added to 20 mL of the dispersion until the total volume reached 100 mL. Afterward, the dispersion was stirred for 2 h at 1500 rpm

and then allowed to rest for 30 min. The transparent carbon layer formed at the interface was then separated from the solution and put onto the FTO glass. The material was dried at 70 °C and sintered at 350 °C for 1 h in a nitrogen atmosphere to form the FTO/C_t counter electrode. For comparison, the FTO/Pt electrode was also synthesized through the addition of several drops of 5 mM H_2PtCl_6 in isopropanol on the FTO glass and then heating at 450 °C for 30 min.

Material characterization. The surface morphologies of the synthesized TiO_2 and transparent carbon electrode were characterized using a Zeiss Evo scanning electron microscope. The optical properties of the electrodes were evaluated via UV–vis and Fourier-transform infrared (FTIR) spectroscopy. X-ray diffraction (XRD) and Raman characterization were also conducted to determine the crystal phase and the structural properties. The electrochemical behavior of the synthesized counter electrodes was determined via cyclic voltammetry using a EdaQ potentiostat, with 0.05 M $K_3Fe(CN)_6$ in 0.1 M KCl at a potential window of −200 to 600 mV. The resistance value of the samples was measured using a digital multimeter.

DSSC fabrication and characterization. First, the FTO/TiO_2 photoanode was sensitized using curcumin dye via overnight immersion in a 3 mM solution (in ethanol). Afterward, the sensitized photoanode was cleaned with pure ethanol to remove the excess dye from the electrode. The DSSC was fabricated by arranging the FTO/TiO_2/curcumin photoanode, spacer material (parafilm), I^-/I_3^- electrolyte, and the counter electrodes in a sandwich structure. The exposed area of the DSSC was approximately 1.5 × 1.5 cm. The DSSC performance was then tested using an *I–V* curve under visible light illumination using a 12 W wolfram lamp as an energy source.

Results and Discussion

Evaluation of the optical and electrical properties of the self-synthesized FTO. The deposition technique was adapted from a previously reported procedure in which a nebulizer was used to systematically coat silica glass with a SnO_2-F layer by layer inside a furnace [20]. The desired FTO substrate needs to possess high conductivity while maintaining high transparency under visible light illumination conditions. The conductivity was represented by the value of sheet resistance calculated using Equation (1):

$$s = R\frac{W}{L} \tag{1}$$

where R_s = sheet resistance (Ω/sq), R = resistance obtained via standard multimeter measurement, W = the FTO width, and L = the distance between two multimeter probes. Table 1 shows that the average R_s of the FTO was 11.68 ± 3.21 Ω/sq.

Figure 1a shows the transmittance profile of the three synthesized FTO substrates compared with that of the glass before FTO deposition, with quartz as a standard. The figure shows that the FTO samples showed acceptable transmittance around 70%–84% in the visible light area (400–800 nm). The basic silica glass used had a 90 %T value compared with quartz glass. Therefore, it can be expected that a higher %T value will be obtained when quartz glass is used as the material.

The thickness of the deposited FTO can be estimated using the Swanepoel Equation (2) [22]:

$$d = \frac{\lambda_1\lambda_2}{2(\lambda_1 n_2 - \lambda_2 n_1)} \tag{2}$$

$$n = \sqrt{N + \sqrt{N^2 - n_s^2}} \tag{3}$$

$$N = 2n_s\frac{T_M - T_m}{T_M T_m} \tag{4}$$

where d is the calculated thickness of the film; λ_1 and λ_2 are the wavelengths at each successive transmittance peak (or valley); and n_1 and n_2 are the refractive indices of the film at wavelengths λ_1 and λ_2, respectively. The refractive index (n) of the prepared FTO layer can be calculated using Equation (3), where n_s is the refractive index of the substrate (in this case, because the substrate is glass, the refraction index is 1.52). T_M and T_m are the maximum and minimum transmittance values at the wavelength corresponding to the transmittance peak or valley, respectively. Figure 1b shows how several units for the calculation were determined.

Table 1. The Summary of the FTO Optical and Electrical Properties

Sample	Average %T	The band gap (eV)	d (nm)	Rs (Ω/sq)
FTO 1	78.37	3.78	523.48	10.52
FTO 2	77.83	3.70	594.10	9.21
FTO 3	81.07	3.72	416.43	15.31
Average	79.09 ± 1.73	3.73 ± 0.04	511.34 ± 89.45	11.68 ± 3.21

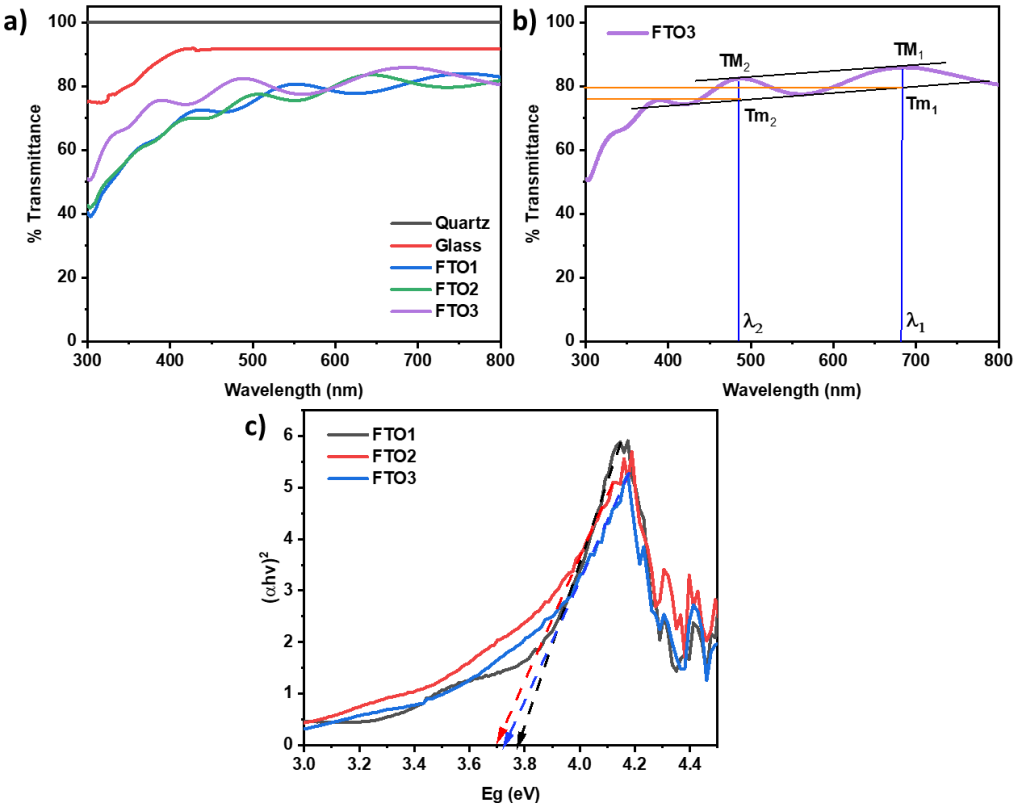

Figure 1. Optical Characteristics of the Synthesized FTO Conductive Glass: a) Transmittance–wavelength Curve Obtained using a UV–vis Spectrometer; b) FTO Thickness Calculated via the Swanepoel Method; c) Band Gap Calculated using Tauc Plot

The *d* value obtained from the Swanepoel calculation was then used to estimate the band gap value of the synthesized FTO using the Tauc Equation (5).

$$\alpha hv = A\,(hv - Eg)^n \quad (5)$$

$$\alpha = \frac{1}{d} ln \frac{1}{T} \quad (6)$$

where α = absorption coefficient, h = planck constant (6,626 × 10^{-34} Js), v = photon frequency (v = c/λ), A = constant, Eg = band gap (eV), T = transmittance, d = layer thickness, and n = ½ for the allowed transition.

The Eg value can be obtained from Equations (5) and (6) and by constructing a relationship curve between $(\alpha hv)^2$ as the y-axis and hv as the x-axis and extrapolating the line to $(\alpha hv)^2 = 0$ (Figure 1c). The optical and electrical evaluation of the synthesized FTO is summarized in Table 1.

Table 1 shows that the results varied to a certain degree even though the same fabrication method was adopted. However, an increase in the thickness of the FTO layer resulted in lower %T and Rs values. Thus, only FTO with an Rs of ~11.68 Ω/sq was used in the subsequent experiment to minimize the error resulting from the FTO resistance difference. The average band gap value was similar to the SnO_2-F values reported in numerous studies, indicating that the synthesized layer was in the form of FTO.

Characterization of the synthesized FTO/TiO_2 photoelectrodes. RBA is a technique for anodizing a Ti plate in chloride or perchlorate media according to electrochemical principles to produce TiO_2 powder with a cluster of nanotube morphology [18,19]. The current generated over the anodization time at a constant anodization potential is depicted in Figure 2a. Generally, the process of forming TiO_2 nanotubes from Ti plates involves four stages: 1) gas formation at the anode and cathode (Equations 7 and 9) along with the formation of a white layer of TiO_2 insulator at the anode (Equation 10; drop current); 2) partial dissolution of the TiO_2 on the anode by the chloride ion formed at the cathode to form pores (Equations 8 and 11), marked by increasing current profile; at this stage, slight tube etching also occurs owing to the mechanical stress between the tube and the Ti plate; 3) the equilibrium stage of formation,

dissolution, and etching (relatively constant current); and 4) the solution saturation stage (drop current); at this stage, the solution becomes saturated from the formation of TiO_2 powder and $[TiCl_6]^{2-}$; moreover, the area of the Ti plate electrode decreases owing to the reaction process. The reactions that occur in the system are as follows:

The reaction at the cathode:

$$2H^+_{(aq)} + 2e \rightarrow H_{2\,(g)} \quad (7)$$

$$ClO_4^-{}_{(aq)} + 8H^+_{(aq)} + 8e^- \rightarrow Cl^-_{(aq)} + 4H_2O_{(l)} \quad (8)$$

The reaction at the anode:

$$2H_2O_{(l)} \rightarrow O_{2\,(g)} + 4e^- + 4H^+_{(aq)} \quad (9)$$

$$Ti_{(s)} + 2H_2O_{(l)} \rightarrow TiO_{2\,(s)} + 4e^- + 4H^+_{(aq)} \quad (10)$$

$$TiO_{2\,(s)} + 4H^+_{(aq)} + 6\,Cl^-_{(aq)} \rightarrow [TiCl_6]^{2-}_{(aq)} + 2H_2O_{(l)} \quad (11)$$

The TiO_2 powder formed was cleaned with hot DI water until it was free from chloride and acid; then it was oven-dried at 60 °C for 24 h and then characterized via scanning electron microscopy (SEM, Figure 2b). The majority of the clusters were bundled, forming large non-uniform particles (Figure 2b). Only small parts, marked with a red circle in Figure 2b, showed a tublike morphology similar to the morphologies reported in [18,19], with surface nanograins. These results are attributable to the unideal reaction conditions such as the stirring process and the exceedingly high-rate etching process, so that TiO_2 was easily released from the Ti surface before the dissolution process during nanotube formation was complete. To address this issue, further optimization of the anodization conditions such as the voltage and acid concentrations might be needed. Moreover, a gentler stirring process and direct separation of the precipitate after anodization is needed. Furthermore, the sonication treatment after the powder cleaning process may also help to separate the aggregate formed by the whole process. These suggestions will be considered in the subsequent study. Nevertheless, the sample powder can still for the crystallization experiment. Two crystallization methods were used (URTC and annealing), and the optical and structural characterization results are shown in Figure 3.

Figure 3a compares the Diffuse Reflectance Spectrometer (DRS) spectra of the crystallized and amorphous samples. The band gap was determined using the Tauc plot (Figure 3b), which showed band gaps of 2.92, 3.10, and 3.14 eV, for amorphous, URTC, and annealed samples, respectively. The band gap energy and reflectance of the amorphous sample were lower than those of the crystallized samples because of the disoriented structure and high defect concentration. The crystallization process made the atomic configuration more ordered, lowering the defect concentration and thus increasing the band gap and reflectance profile [23, 24].

All TiO_2 samples exhibited three main infrared absorptions modes (Figure 3c). The peak at 400–850 cm^{-1} suggests that the amorphous sample exhibited a weaker Ti–O–Ti bond vibration than the crystallized sample. The peaks at 1500–1700 cm^{-1} and 3000–3700 cm^{-1}, corresponding to the bending and stretching vibrations of the –OH bonds, decreased after crystallization. These results indicate that the 3 h URTC process exhibited a comparable performance to the annealing method for producing a crystal structure by increasing the number of Ti–O–Ti bonds and reducing the number of –OH bonds [25]. The results are consistent with the XRD results (Figure 3d). The amorphous samples exhibited typical anatase 2θ peaks at around 25°, 37°, 48°, 62°, and 75° with low intensities, according to JCPDS card 21-1272 [26]. After crystallization, the intensity of the peaks increased, and a new 2θ peak was formed at 82.4°, which was not previously detected in the amorphous samples. The intensities of the characteristic peaks of rutile and brookite were also strengthened. This indicates that the sample transformed into the anatase crystalline phase, with a small amount of rutile and brookite. The average crystallite size of the annealed sample calculated using Scherer's equation was 11.60 ± 2.37 nm, while the size of the URTC sample was 10.08 ± 2.52 nm.

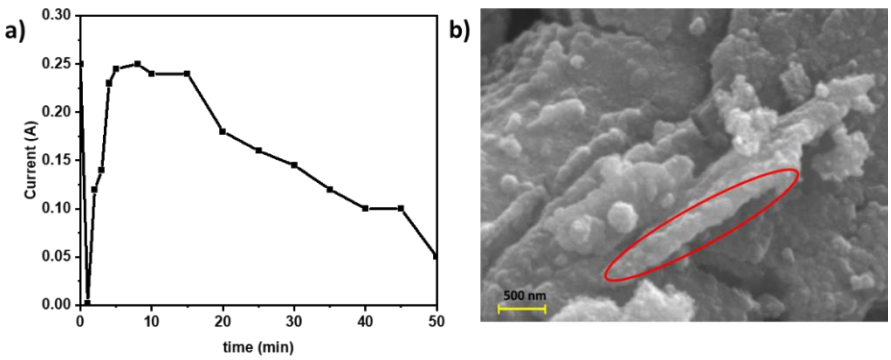

Figure 2. a) Anodization Curve of Titanium Plate; b) SEM Image of TiO_2 Formed via the RBA Technique

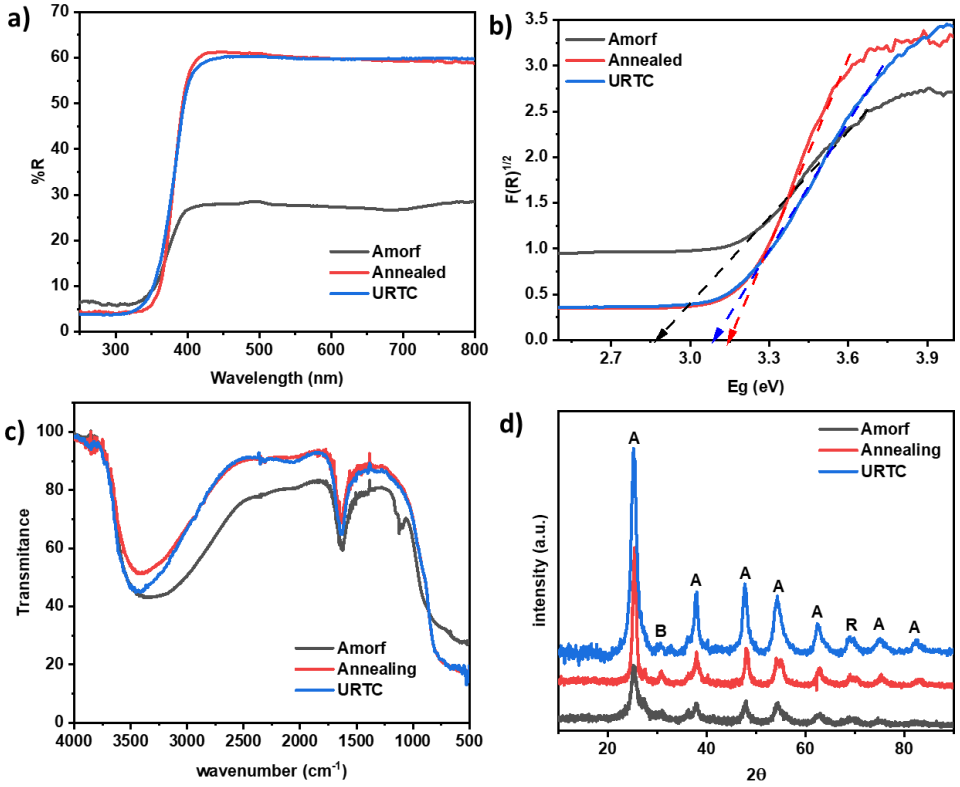

Figure 3. The Optical and Structural Characteristics of TiO_2 Powder Before and After Crystallization: a) UV–vis DRS spectra; b) Tauc Plot for Band Gap Calculation; c) FTIR Spectra; d) X-ray Diffractograms

The TiO_2 samples were then deposited on FTO glass via the doctor blade method, and the photocurrent response was examined via multipulse amperometry. For convenience, the annealed TiO_2 sample was labeled TiO_2a, while the URTC-prepared TiO_2 sample was labeled TiO_2u. Figure 4a compares the FTO/TiO_2u electrode and FTO/TiO_2a under UV light illumination. The results indicate that FTO/TiO_2a slightly outperformed FTO/TiO_2u, possibly because the crystallization degree of URTC was still lacking compared with the annealing process, as shown by the higher intensity of the –OH stretching absorbance peak in the FTIR spectrum, less sharp XRD peak (wider WFHM value), and smaller crystallite size of the URTC sample compared with the annealed sample [27]. The FTO/TiO_2 electrodes were then immersed in curcumin solution, and the photocurrent responses under visible light illumination were recorded. The results (Figure 4b) show the high photocurrent activity of the sensitized TiO_2u electrode compared with the pristine TiO_2 under visible light. Furthermore, the performance of TiO_2u was comparable to that of the curcumin-sensitized TiO_2a photoanode. However, the photocurrent gain decreased over time, owing to the degradation of curcumin dyes under irradiation in aqueous media [28]. Thus, the presence of water is strictly prohibited in DSSC fabrication.

Evaluation of FTO/transparent carbon (FTO/C_t) counter electrode. The DSSC counter electrode plays an important role as the electron collector to regenerate the excited sensitizer under illumination. Thus, the high-efficiency catalyst should be deposited on the FTO surface to enhance electron transfer. A conductive transparent carbon layer can be formed using a liquid–liquid interface by leveraging the interfacial force of two immiscible solvents [12]. Figure 5a shows an SEM image of a transparent carbon layer deposited on FTO, while the inset shows the film before the deposition. The figures show that the films exhibited low homogeneity. An imperfect dispersion process at the initial step can cause this non-uniformity. The self-assembly process of the carbon film when the mixed system was rested after mixing is also a factor. External shocks can cause the formation of an uneven layer of carbon film [12, 29]. Several suggestions that might help to boost the quality of the carbon film formed include pretreatment of graphite before use, further optimization of the solvent variation and ratio, and minimization of the shocks in the resting and deposition process. However, in this study, the FTO/C_t electrode formed was used as it is and then compared with bare FTO and the FTO/Pt electrode.

Figure 5b shows the optical characteristics of the fabricated counter electrodes. The catalyst deposition

generally reduced the optical transmittance of the electrode. FTO/C_t exhibited a lower transmittance than the other electrodes. Figure 5c provides the Raman spectra of the three electrodes. The FTO spectra show distinct characteristics of broad peaks around 300–780 cm^{-1}. Specifically, the peaks at approximately 475, 630, and 780 cm^{-1} correspond to the E_g, A_{1g}, and B_{2g} vibration modes of rutile SnO_2, respectively. The fluorine doping effect was marked by the formation of the 410 cm^{-1} A_{2g} Raman mode [30]. The peak around 1000 cm^{-1} can be ascribed to the CaO–SiO_2 vibration mode of the fused silica glass used as the basic substrate [31]. The Pt and C_t coating on FTO glass made these peaks unobserved. However, the FTO/C_t Raman spectra featured three dominant peaks, at 1335,1580, and 2700 cm^{-1}, which correspond to the D, G, and 2D bands of graphite, respectively. The samples showed higher absorption of the G band than the D band, suggesting that most of the carbon featured an sp^2 morphology, rather than an amorphous structure, consistent with the occurrence of different conductivity degrees on the FTO plate, as sp^2 carbon can conduct electricity [32].

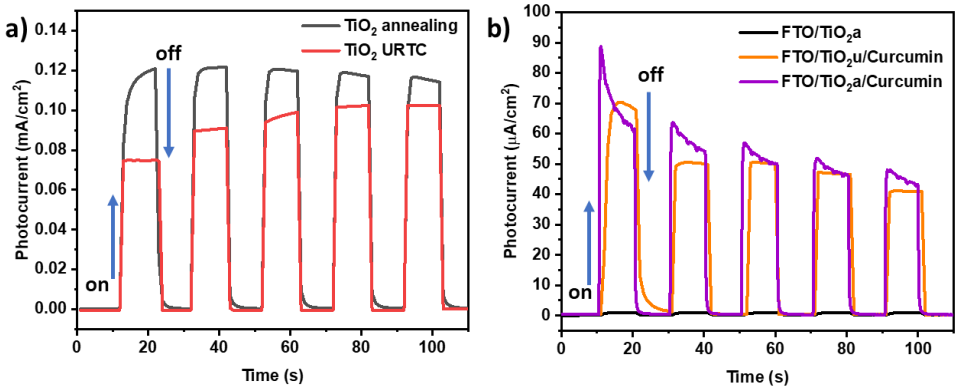

Figure 4. Photocurrent Response of the Fabricated Photoelectrodes Obtained via Multipulse Amperometry in 0.1 M Na_2SO_4 at 0 V vs. Ag/AgCl; a) Chopped UV Black Light; b) Chopped Visible Light

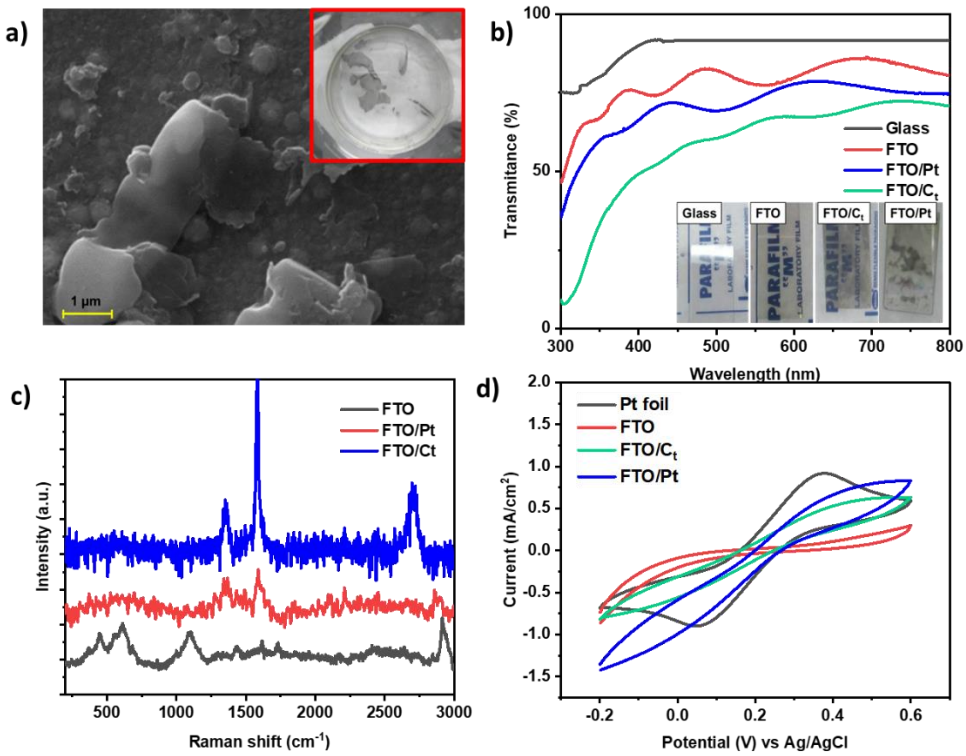

Figure 5. Counter Electrode Characteristics: a) SEM Morphology of the FTO/C_t Electrode; Inset: Physical Map of the C_t Layer Before Deposition; b) Physical Maps and Transmittance Profile of the Electrodes; c) Raman Spectra; d) Curve of CV in $K_3Fe(CN)_6$ Solution at 100 mV/s Scan Rate

The optical and electrical characteristics of the electrodes are given in Table 2. According to the table, the Pt-coated glass exhibited a lower average sheet resistance than the uncoated glass. This indicates that the conductivity of the glass increased as the platinum metal was deposited on FTO. However, the resistance of the C_t-coated glass sheet was higher than that of the uncoated sheet. The increase in sheet resistance indicates the unevenness of the resulting carbon film. The conductivity of the carbon layer considerably varied with the layer thickness and quality, which are also greatly affected by the quality of the precursor used. Although the sheet resistance increases, this deficiency can be compensated for because carbon has a large surface area to provide more catalytic space. In addition, the carbon–FTO electron conduction band is characterized by a high film conductivity and a large active cross-sectional area. A cyclic voltammetry test was conducted to confirm this hypothesis. The FTO electrode was used as the working electrode to conduct a reversible reaction of Ferry cyanide ions. The peaks of Fe^{2+} oxidation to Fe^{3+} are expected to correspond to a potential of around +0.4 V, while the peaks of Fe^{3+} reduction to Fe^{2+} are expected to correspond to at ~0 V vs. Ag/AgCl [33]. Figure 5d shows that the FTO/C_t exhibited a higher current response than bare FTO, indicating the transparent carbon-bearing FTO surface enhanced electron transfer from the electrode to the system [34]. Although the system was still inferior compared with FTO/Pt, a comparable result can be obtained by further developing the optimization method.

Performance evaluation of the fabricated curcumin-based DSSC. The DSSCs were assembled according to a sandwich arrangement of sensitized photoanodes, electrolytes, and counter electrodes. In the middle of the cell, a parafilm spacer with a thickness of 2 mm was added to separate the (+) and (−) poles of the solar cell to prevent direct electron transfer between the two electrodes. The performance was evaluated by measuring the *I* vs. *V* curve under front and back illumination conditions. This study focused on three types of DSSCs: 1) A DSSC with annealed curcumin-sensitized TiO_2 as the photoanode and Pt-coated FTO (TiO_2a–FTO/Pt) as the counter electrode (the standard system). 2) A DSSC with URTC-prepared curcumin-sensitized TiO_2 as the photoanode and FTO/transparent carbon (TiO_2u–FTO/C_t) as the counter electrode. 3) A DSSC with annealed curcumin-sensitized TiO_2 as the photoanode and bare FTO (TiO_2a–FTO) as the counter electrode.

Figure 6 shows the photocurrent response of the fabricated DSSCs. Front irradiation was conducted with the photoanode facing the light source, while for back-irradiation, the light first hit the counter electrode. The power input for all measurements was fixed at 0.308 mW/cm^2. The short circuit current (J_{sc}), open circuit potential (V_{oc}), and maximum power output (P_{max}) values can be determined from the curve. J_{sc} is the current generated when the potential between the electrodes is 0, while V_{oc} is the potential of the cells when no current can flow. The fill factor (FF) and efficiency of the cells were also calculated using Equations (12) and (13). The overall performance of the fabricated solar cells is summarized in Table 3.

$$FF = \frac{J\max x\, Vmax}{Jsc\, x\, Voc} \tag{12}$$

$$\eta = \frac{Pmax}{P\ in} \times 100\% \tag{13}$$

The FF measures how much the DSSC system can maximize its maximum potential. The FF value is dependent on the overall resistance of the system from the photoanode, electrolyte, to the counter electrode. The counter electrode acts as a system to transfer electrons from the external circuit back to the internal system to regenerate holes in the electrolyte. Under a high electron regeneration ability, the system circulation will run well; therefore, the FF will be higher [10]. According to the measurements and calculation, TiO_2a-FTO/Pt exhibited the highest FF and efficiency. TiO_2u-FTO/C_t showed comparable performance to TiO_2a-FTO/Pt and

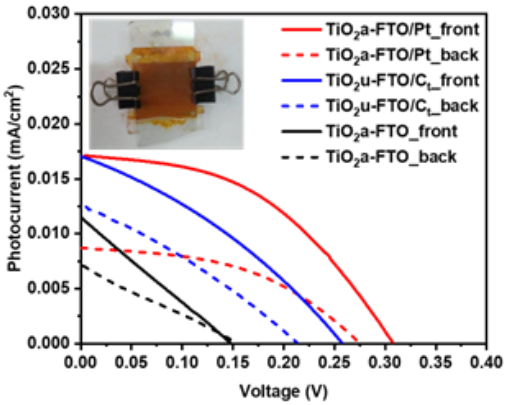

Figure 6. The Physical Map and I–V Curve of the Fabricated DSSC

Table 2. The Optical and Electrical Characteristics of the Counter Electrodes

Sample	R_s of original FTO (Ω/sq)	Rs after coating (Ω/sq)	Average %T
FTO	10.52	10.52	78.23
FTO/Pt	11.72	9.65	69.91
FTO/C_t	11.55	23.62	58.26

Table 3. The Overall Performance of the Fabricated DSSC

DSSC construction	Vmax (mV)	Imax ($\mu A/cm^2$)	Jsc ($\mu A/cm^2$)	Voc (mV)	FF	Pmax ($\mu W/cm^2$)	η (%)
TiO_2a_Pt *front*	190	8.38	11.4	308	0.454	1.593	0.52
TiO_2a _Pt *back*	174	6.31	8.68	275	0.460	1.097	0.36
TiO_2u_C *front*	146	9.86	16.99	258	0.328	1.44	0.47
TiO_2u_C *back*	110	7.32	12.49	214	0.301	0.806	0.26
TiO_2a_FTO *front*	74	5.70	11.51	147	0.249	0.422	0.14
TiO_2u_FTO *back*	84	3.32	9.35	155	0.192	0.278	0.09

considerably outperformed TiO_2a-FTO. The results demonstrate the potential of the URTC technique with transparent carbon as the counter electrode as an alternative to the established DSSC fabrication procedure.

Furthermore, the DSSC yielded better results under front illumination compared with back illumination conditions, because at front illumination, the light source was in direct contact with the photoanode, and the energy was used to excite the electron close to the maximum level. However, at back illumination conditions, the light source passed through the counter electrode and the I^-/I_2 electrolyte, which caused a decrease in light intensity before contact with the photoanode. Thus, to further improve the DSSC performance under back illumination conditions, increasing the counter electrode's transparency and conductivity is necessar

Conclusions

This work investigated alternative techniques to reduce DSSC production costs by providing results that are not much different from those of standard fabrication methods. The URTC technique was used to crystallize amorphous TiO_2 and yielded comparable crystallite size and photocurrent activity to those of the TiO_2 crystallized via the conventional heating method. Moreover, through a liquid–liquid interface technique, a transparent carbon counter electrode with higher catalytic activity than bare FTO and only slightly lower conductivity than FTO/Pt was successfully synthesized. The following results were achieved even under the imperfect condition of the FTO/C_t counter electrode: uneven carbon layer distribution, low transmittance, and high sheet resistance. These results are attributable to the high active area of the transparent carbon layer and the good intrinsic properties of the carbon material. Finally, the curcumin-based DSSC fabricated using the URTC-prepared TiO_2 photoanode coupled with the FTO/C_t counter electrode exhibited comparable FF and efficiency to the electrode fabricated via standard methods. Thus, further development and optimization of the crystallization technique and transparent carbon fabrication techniques, particularly to improve film conductivity and transparency, is recommended.

Acknowledgments

This research was funded and supported by the cluster research scheme from University of Indonesia [Titania photo electro catalysis (TiPEC)] contract number: 1864/UN2.R12/HKP.05.00/2015), and also PMDSU batch IV grant scheme 2020

References

[1] Khanna, S., Sundaram, S., Reddy, K.S., Mallick, T.K. 2017. Performance analysis of perovskite and dye-sensitized solar cells under varying operating conditions and comparison with monocrystalline silicon cell. Appl. Therm. Eng. 127: 559–565, https://doi.org/10.1016/j.applthermaleng.2017.08.030.

[2] Nazeeruddin, M.K., Baranoff, E., Grätzel, M. 2011. Dye-sensitized solar cells: A brief overview. Sol. Energy. 85(6): 1172–1178, https://doi.org/10.1016/j.solener.2011.01.018.

[3] Chander, S., Purohit, A., Sharma, A., Nehra, S.P., Dhaka, M.S. 2015. Impact of temperature on performance of series and parallel connected mono-crystalline silicon solar cells. Energy Rep. 1: 175–180, https://doi.org/10.1016/j.egyr.2015.09.001.

[4] Sharma, K., Sharma, V., Sharma, S.S. 2018. Dye-Sensitized Solar Cells: Fundamentals and Current Status. Nanoscale Res. Lett. 13: 381, https://doi.org/10.1186/s11671-018-2760-6.

[5] Asghar, A., Emziane, M., Pak, H.K., Oh, S.Y. 2014. Outdoor testing and degradation of dye-sensitized solar cells in Abu Dhabi. Sol. Energy Mater. Sol. Cells. 128: 335–342, https://doi.org/10.1016/j.solmat.2014.05.048.

[6] Cui, Y., Yao, H., Zhang, J., Zhang, T., Wang, Y., Hong, L., *et al*. 2019. Over 16% efficiency organic photovoltaic cells enabled by a chlorinated acceptor with increased open-circuit voltages. Nat. Commun. 10: 2515, https://doi.org/10.1038/s41467-019-10351-5.

[7] Kakiage, K., Aoyama, Y., Yano, T., Oya, K., Fujisawa, J.I., Hanaya, M. 2015. Highly-efficient dye-sensitized solar cells with collaborative sensitization by silyl-anchor and carboxy-anchor dyes. Chem. Commun. 51(88): 15894–15897, https://doi.org/10.1039/c5cc06759f.

[8] Snaith, H.J. 2009. Estimating the Maximum Attainable Efficiency in Dye-Sensitized Solar Cells. Adv. Funct. Mater. 20(1): 13–19, https://doi.org/10.1002/adfm.200901476.

[9] Xiong, D., Chen, W. 2012. Recent progress on tandem structured dye-sensitized solar cells. Front Optoelectron. 5: 371–389, https://doi.org/10.1007/s12200-012-0283-9.

[10] Kumar, R., Nemala, S.S., Mallick, S., Bhargava, P. 2017. High efficiency dye sensitized solar cell made by carbon derived from sucrose. Opt. Mater. 64: 401–405, https://doi.org/10.1016/j.optmat.2017.01.013.

[11] Lim, J., Ryu, S.Y., Kim, J., Jun, Y. 2013. A study of TiO_2/carbon black composition as counter electrode materials for dye-sensitized solar cells. Nanoscale Res. Lett. 8: 227, https://doi.org/10.1186/1556-276X-8-227.

[12] Souza, V.H.R., Flahaut, E., Zarbin, A.J.G. 2017. Conducting, transparent and flexible substrates obtained from interfacial thin films of double-walled carbon nanotubes. J. Colloid Interface Sci. 502: 146–152, https://doi.org/10.1016/j.jcis.2017.04.084.

[13] Yunita, Syauqi, M.I., Gunlazuardi, J. 2022. Comparative Study of Bismuth Ferrite Deposition Method on TiO_2 Nanotube and Performance of Hydrogen Evolution in a Photoelectrochemical Dye-Sensitized Solar Cell Tandem System. Makara J. Sci. 26(3): 190–199, https://doi.org/10.7454/mss.v26i3.1387.

[14] Pari, B., Chidambaram, S., Kasi, N., Sivakumar, S. 2013. Recent Advances in SnO_2 Based Photo Anode Materials for Third Generation Photovoltaics. Mater. Sci. Forum. 771: 25–38, https://doi.org/10.4028/www.scientific.net/MSF.771.25.

[15] Tang, Y., Wu, Z., Li, C. 2016. Efficient CdS/N719 Cosensitized Solar Cells Based on ZnO Nanorod Arrays. 2016. Synth. React. Inorganic, Met. Nano-Metal Chem. 46(11): 1691–1694, https://doi.org/10.1080/15533174.2015.1137046.

[16] Liao, Y., Que, W., Zhong, P., Zhang, J., He, Y. 2011. A facile method to crystallize amorphous anodized TiO_2 nanotubes at low temperature. ACS Appl. Mater. Interfaces. 3(7): 2800–2804, https://doi.org/10.1021/am200685s.

[17] Lamberti, A., Chiodoni, A., Shahzad, N., Bianco, S., Quaglio, M., Pirri, C.F. 2015. Ultrafast Room-Temperature Crystallization of TiO_2 Nanotubes Exploiting Water-Vapor Treatment. Sci. Rep. 5: 7808, https://doi.org/10.1038/srep07808.

[18] Antony, R.P., Mathews, T., Dasgupta, A., Dash, S., Tyagi, A.K., Raj, B. 2011. Rapid breakdown anodization technique for the synthesis of high aspect ratio and high surface area anatase TiO_2 nanotube powders. J. Solid State Chem. 184(3): 624–632, https://doi.org/10.1016/j.jssc.2011.01.020.

[19] Ali, S., Granbohm, H., Lahtinen, J., Hannula, S.P. 2018. Titania nanotubes prepared by rapid breakdown anodization for photocatalytic decolorization of organic dyes under UV and natural solar light. Nanoscale Res. Lett. 13: 179, https://doi.org/10.1186/s11671-018-2591-5.

[20] Supriyono, Surahman. H., Krisnandi, Y.K., Gunlazuardi, J. 2015. Preparation and Characterization of Transparent Conductive SnO_2-F Thin Film Deposited by Spray Pyrolysis: Relationship between Loading Level and Some Physical Properties. 2015. Procedia Environ. Sci. 28:242–51, https://doi.org/10.1016/j.proenv.2015.07.031.

[21] Bu, C., Liu, Y., Yu, Z., You, S., Huang, N., Liang, L., *et al*. 2013. Highly Transparent Carbon Counter Electrode Prepared via an in Situ Carbonization Method for Bifacial Dye-Sensitized Solar Cells. 2013. ACS Appl. Mater. Interfaces. 5(15): 7432–7438, https://doi.org/10.1021/am4017472.

[22] Swanepoel, R. 1983. Determination of the thickness and optical constants of amorphous silicon. J. Phys. E. Sci. Instrum. 16: 1214–1222, https://doi.org/10.1088/0022-3735/16/12/023.

[23] Zhu, L., Lu, Q., Lv, L., Wang, Y., Hu, Y., Deng, Z., *et al*. 2017. Ligand-free rutile and anatase TiO_2 nanocrystals as electron extraction layers for high performance inverted polymer solar cells. RSC Adv. 7(13): 20084–20092, https://doi.org/10.1039/c7ra00134g.

[24] Kéri, O., Kocsis, E., Karajz, D.A., Nagy, Z.K., Parditka, B., Erdélyi, Z., *et al*. 2021. Photocatalytic Crystalline and Amorphous TiO_2 Nanotubes Prepared by Electrospinning and Atomic Layer Deposition. Molecules. 26(19): 5917, https://doi.org/10.3390/molecules26195917.

[25] Budiman, H., Wibowo, R., Zuas, O., Gunlazuardi, J. 2019. Photo-electrochemical properties of $TiOs_2$ nanotube arrays: Effect of different polishing method of Ti substrate prior to anodization in fluoride-H_2O_2-containing electrolyte. J. Phys. Conf. Ser. 1153: 012073, https://doi.org/10.1088/1742-6596/1 153/1/012073.

[26] Reyes-Coronado, D., Rodríguez-Gattorno, G., Espinosa-Pesqueira, M.E., Cab, C., De Coss, R., Oskam, G. 2008. Phase-pure TiO_2 nanoparticles: Anatase, brookite and rutile. Nanotechnology. 19: 14, https://doi.org/10.1088/0957-4484/19/14/145605.

[27] Wu, Y.C., Hung, C.K., Tsai, C.Y., Guo, Y.L., Chiang, Y.H., Chen, P. 2017. Clean and flexible synthesis of TiO_2 nanocrystallites for dye-sensitized and perovskite solar cells. 2017. Sol. Energy. Mater. Sol. Cells. 159: 336–344, https://doi.org/10.1016/j.solmat.2016.09.033.

[28] Lu, H.L., Shen, T.F.R., Huang, S.T., Tung, Y.L., Yang, T.C.K. 2011. The degradation of dye sensitized solar cell in the presence of water isotopes. Sol. Energy. Mater. Sol. Cells. 95(7): 1624–1629, https://doi.org/10.1016/j.solmat.2011.01.014.

[29] Salvatierra, R.V., Cava, C.E., Roman, L.S., Zarbin, A.J.G. 2013. ITO-Free and Flexible Organic Photovoltaic Device Based on High Transparent and Conductive Polyaniline/Carbon Nanotube Thin Films. Adv. Funct. Mater. 23(12): 1490–1499, https://doi.org/10.1002/adfm.201201878.

[30] Haddad, N., Ben Ayadi, Z., Mahdhi, H., Djessas, K. 2017. Influence of fluorine doping on the microstructure, optical and electrical properties of SnO2 nanoparticles. J. Mater. Sci. Mater. Electron. 28: 15457–15465, https://doi.org/10.1007/s10854-017-7433-1.

[31] Han, C., Chen, M., Rasch, R., Yu, Y., Zhao, B. 2016. Structure Studies of Silicate Glasses by Raman Spectroscopy. Adv. Molten Slags, Fluxes, Salts Proc. In: Reddy, R.G., Chaubal, P., Pistorius, P.C., Pal, U. (eds.), Advances in Molten Slags, Fluxes, and Salts: Proceedings of the 10th International Conference on Molten Slags, Fluxes and Salts 2016. Springer. Cham. pp. 175–182.

[32] Ferrari, A.C. 2007. Raman spectroscopy of graphene and graphite: Disorder, electron-phonon coupling, doping and nonadiabatic effects. Solid State Commun. 143(1–2): 47–57, https://doi.org/10.1016/j.ssc.2007.03.052.

[33] Putri, Y.M.T.A., Gunlazuardi, J., Ivandini, T.A. 2022. Electrochemical Preparation of Highly Oriented Microporous Structure Nickel Oxide Films as Promising Electrodes in Urea Oxidation. 2022. Chem. Lett. 51(2): 135–138, https://doi.org/10.1246/cl.210634.

[34] Sturdza, B.K., Lauritzen, A.E., Zhou, S., Bennett, A.J., Form, J., Christoforo, M.G., *et al*. 2022. Improving performance of fully scalable, flexible transparent conductive films made from carbon nanotubes and ethylene-vinyl acetate. 2022. Energy Rep. 8(11): 48–60, https://doi.org/10.1016/j.egyr.2022.05.047.